Interaction between bilirubin oxidase and Au nanoparticles distributed over dimpled titanium foil towards oxygen reduction reaction

Wiktoria Lipińska, Vita Saska, Katarzyna Siuzdak, Jakub Karczewski, Karol Zaleski, Emerson Coy, Anne de Poulpiquet, Ievgen Mazurenko, Elisabeth Lojou

Interaction between bilirubin oxidase and Au nanoparticles distributed over dimpled titanium foil towards oxygen reduction reaction

Wiktoria Lipińska[1], Vita Saska[2], Katarzyna Siuzdak[1], Jakub Karczewski[3], Karol Załęski[4], Emerson Coy[4], Anne de Poulpiquet[2], Ievgen Mazurenko[2], Elisabeth Lojou[2]*

[1] Centre for Plasma and Laser Engineering, The Szewalski Institute of Fluid-Flow Machinery, Polish Academy of Sciences, Fiszera 14 St., 80-231, Gdańsk, Poland

[2] Aix Marseille Univ, CNRS, BIP, Bioénergétique et Ingénierie des Protéines, UMR 7281, 31, chemin Joseph Aiguier, CS 70071 13402 Marseille cedex 09, France

[3] Institute of Nanotechnology and Materials Engineering, Faculty of Applied Physics and Mathematics, Gdańsk University of Technology, Narutowicza 11/12 St., 80-233 Gdańsk, Poland

[4] NanoBioMedical Centre, Adam Mickiewicz University, Wszechnicy Piastowskiej 3, 61-614 Poznań, Poland

Corresponding author* lojou@imm.cnrs.fr

Abstract

Spatial distribution of enzymes on electrodes is a key point to understand and optimize bioelectrocatalysis, although not largely investigated. In this work, Ti nanodimples serve as a platform for getting a controlled spatial distribution of gold nanoparticles (AuNPs). By varying the thickness of the initial gold layer, AuNPs with average sizes ranging from 13±6, 46±12 to 81±13 nm are obtained. AFM and TEM allow to localize the AuNPs in the dimples. It is in particular highlighted that the smallest NPs are present not only at the bottom but also on the edges of the Ti dimple, with TiO_2 layer in their close surrounding. Enzymatic O_2 reduction by immobilized *Myrothecium verrucaria* bilirubin oxidase (*Mv* BOD) is then investigated on the different materials. After having demonstrated the occurrence of the bioelectrocatalytic reaction on AuNPs excluding the Ti surface, the efficiency of the catalysis is discussed as a function of the AuNP size. The shape and fitting of the cyclic voltammetry curves obtained with the smallest AuNPs suggest a decrease in the electron transfer rate as a consequence of the colocalization of AuNPs and semiconducting TiO_2. Interestingly, high stability of the

enzymatic current is obtained with the highest AuNPs even in the presence of high concentration of salts.

KEYWORDS: Au nanoparticles; Electrode nanostructuration; Enzymes; Catalysis; Self-Assembled-Monolayers; Bioelectrochemistry; Bilirubin oxidase

1. Introduction

Redox enzymes are very active and extremely selective catalysts toward specific reactions allowing their use in bioelectrochemical devices such as biosensors, bioreactors or biofuel cells [1, 2]. Multi-copper oxidases (MCO) are among the most explored ones because of their ability to oxygen reduction reaction (ORR) into water [3]. Within MCO family, apart from laccases [4, 5] and copper efflux oxidases [6], bilirubin oxidases (BOD) are characterized by high activity and stability at neutral pH with low overpotential towards ORR [7-9]. BODs contain four copper centers, namely a Cu T1 center and a trinuclear center (TNC) composed of Cu T2 and T3. ORR by BOD at an electrochemical interface involves a first electron transfer from the electrode to Cu T1 site, intramolecular electron transfer from Cu T1 to TNC site and finally O_2 reduction to H_2O at the TNC [10, 11]. One challenge remains the electron channeling from the electrode to the Cu T1 binding site of immobilized enzymes. Gold and carbon-based are the most popular electrode materials for such efficient immobilization [12-16]. Further application of nanomaterials such as carbon nanotubes, nanoporous gold and gold nanoparticles (AuNP), increases surface area, hence potential anchorage sites for enzyme immobilization, leading to enhanced catalytic currents. Furthermore, depending on their shape and size, nanomaterials can impact the conformation of proteins hence their stability [17, 18]. Last, nanomaterials can be chemically modified to introduce additional functional groups on the surface and tune the interfacial properties for the grafting of enzymes in a conformation suitable for electrocatalysis. In the particular case of AuNPs, such functionalization can be efficiently realized through self-assembled-monolayers (SAM) of thiols [19-22]. Using this strategy, it was especially highlighted the role of electrostatic interactions in the oriented immobilization of the fungal *Myrothecium verrucaria* BOD (*Mv* BOD) toward a high number of molecules catalyzing O_2 reduction with a high turnover [23]. It was also shown an optimum enzyme coverage for electrocatalysis between rigid monolayer and protein crowding [21, 24]. But the reason underlying this observation is still obscure. To get insight into this, surface patterning may allow tuning in a controlled manner the spatial distribution of enzymes on the surface [25].

Toward this goal, a nanosecond laser interaction with nanometric gold films deposited on indium tin oxide (ITO) support was performed to generate *in situ* AuNPs with different sizes and densities [26]. However, the size of the obtained nanoparticles prevented any study on the effect of the enzyme coverage on the electrocatalysis. Moreover, the ITO substrate itself was shown to allow MCO-based catalysis, complexifying the analysis of the electrochemical signal.

Another way to generate AuNPs is the furnace [27] or laser dewetting [28] of thin gold films sputtered over a nanostructured titanium platform received by chemical etching of previously anodized TiO_2 nanotubes. The anodization process followed by chemical etching of TiO_2 nanotubes leads to the formation of well-organized array of Ti dimples that reproduce the bottom part of nanotubes. Following the dewetting process, AuNPs are located in the Ti dimples, their size being less than 100 nm. Such electrodes were previously applied for glucose detection by glucose oxidase embedded in chitosan matrix [28]. The objective was mainly towards enhanced performances of glucose biosensing, and no tuning of the AuNPs size was researched. As far as we know, no study on other enzymes deposited on AuNPs formed on nanostructured titanium foil has been reported.

The goal of the current work is to study *Mv* BOD immobilization on various sizes of AuNPs deposited on nanostructured Ti platform, and evaluate the effect on enzyme activity toward ORR. The size of AuNPs was controlled by the thickness of the gold layer sputtered onto the dimpled Ti substrate. After in depth characterization of the nanomaterials, the electrocatalytic activity of the electrode material with anchored *Mv* BOD was evaluated via cyclic voltammetry and chronoamperometry measurements. It is proved that the thickness of the initial gold film and in consequence the size of AuNPs used for further enzyme immobilization has a significant influence on the catalytic current both in terms of rate of the interfacial electron transfer process and on the stability of the bioelectrocatalytic signal in high ionic strength electrolytes.

2. Experimental

2.1. Materials and Reagents

Titanium foil (99.7 %, Strem), acetone (99.5 %, Chempur), ethanol (96 %, Chempur), ammonium fluoride (98%, Chempur), ethylene glycol (99%, Chempur), oxalic acid dihydrate (99.5%, Sigma-Aldrich) were used for anodization process of Ti and further chemical etching of as-anodized Ti plates. Gold target (99.99%, Quorum Technologies) was used for thin gold layer deposition. 6-mercaptohexanoic acid (6-MHA) (Sigma Aldrich) and bilirubin oxidase

from *Myrothecium verrucaria* (*Mv* BOD) (kind gift from Amano Enzymes Inc. Nagoya, Japan) were used for the AuNPs/Ti electrode modification. Disodium hydrogen phosphate and sodium dihydrogen phosphate (99.0 %, Chempur), potassium ferricyanide $K_3[Fe(CN)_6]$ and potassium ferrocyanide $K_4[Fe(CN)_6]$ from Sigma, hexaammineruthenium (II) chloride $Ru(NH_3)_6Cl_2$ from Thermo Scientific and hexaammineruthenium (III) chloride $Ru(NH_3)_6Cl_3$ from Sigma were used for electrochemical tests. All solutions were prepared with Milli-Q water.

2.2. Electrode Preparation

Firstly, Ti foil was cut into 2×3 cm^2 plates and then ultrasonically cleaned. Secondly, TiO_2 nanotubes were prepared through two-step anodization process and then chemically etched in the oxalic acid solution forming Ti nanodimples (Ti) [27, 29]. Thirdly, the nanostructured titanium foil was covered by different thicknesses of gold, namely 2 nm, 5 nm, 10 nm and 15 nm, using magnetron sputtering machine (Q150T S system, Quorum Technologies) and pure gold plate as a target. Then electrodes were annealed at 450°C for 10 minutes in muffle furnace (MidiSUN KXP3 ET, Neoterm). Depending of the initial gold thickess different morphologies of the material were provided. In the current manuscript, the electrodes are labelled as following: 2Au@Ti, 5Au@Ti, 10Au@Ti and 15Au@Ti for Ti covered by respectively 2 nm, 5 nm, 10 nm and 15 nm Au layer. The catalytic efficiency of the so-fabricated electrodes was compared to a typical disc gold electrode (labelled as Audisc) from pure gold and manufactured by Mineral with a geometrical surface area of 0.0314 cm^2. Ti electrodes after thermal treatment of the film sputtered on or pure nanostructured Ti substrate were chemically modified by incubation during night in 5 mM 6-MHA solution dissolved in ethanol. For enzyme adsorption, electrodes were incubated for 15 min at 4°C in freshly prepared enzyme solution in 100 mM phosphate buffer (PBS) pH 6. Increasing *Mv* BOD concentrations from 2 nM, 200 nM, 500 nM, 2 µM, 20 µM, 50 µM, up to 100 µM were studied. Bioelectrodes were then gently washed with 100 mM phosphate buffer solution pH 6 to remove the loosely adsorbed enzymes before transfer to the electrochemical cell containing 100 mM phosphate buffer pH 6 for further electrocatalytic experiments. Electrodes are inserted in a special home made holder for connection to the potentiostat, and partially covered by parafilm defining a surface area in contact with the electrolyte equal to ca. 0.6 cm^2. The final material was labelled as BOD-M-XAu@Ti, where X stands for the thickness of the initial gold film, and M for 6-MHA modification. Scheme 1 illustrates the fabrication process of the electrodes used throughout this work, and the detailed description of the various electrodes with their respective names is summarized in Table 1.

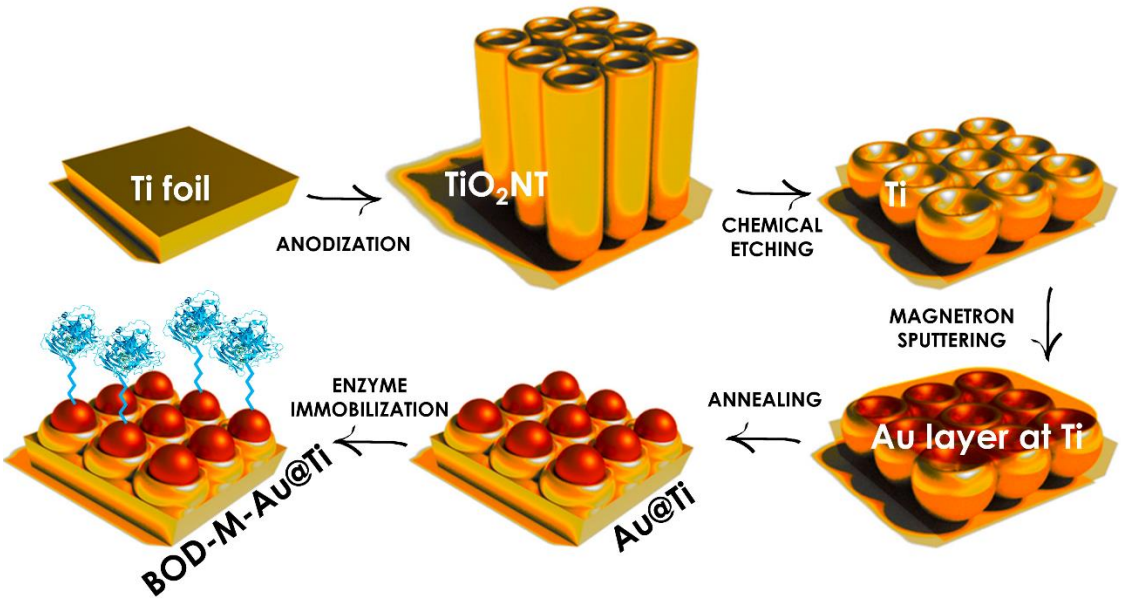

Scheme 1. Schematic fabrication process of enzyme modified Au@Ti electrodes.

Table 1. Description and denomination of the various electrodes.

Electrode (M: SAM, X: thickness of the initial gold layer)		**Description**
XAu@Ti	2Au@Ti, 5Au@Ti, 10Au@Ti, 15Au@Ti	Au nanoparticles deposited on Ti nanodimples
M-XAu@Ti	M-2Au@Ti, M-5Au@Ti, M-10Au@Ti	Thiol modified Au NPs deposited on Ti nanodimples
BOD-M-XAu@Ti	BOD-M-2Au@Ti, BOD-M-5Au@Ti, BOD-M-10Au@Ti	Enzyme immobilized on SAM-modified Au NPs deposited on Ti nanodimples
M-Ti		Thiol modified Ti nanodimples without gold
BOD-M-Ti		Enzyme and thiol modified Ti nanodimples without gold
BOD-M-Audisc		Enzyme and thiol modified Audisc electrode

2.3. Morphology characterization

The morphology of 2Au@Ti, 5Au@Ti, 10Au@Ti and 15Au@Ti was investigated by scanning electron microscope (SEM) (FEI Quanta FEG 250) equipped with Everhart–Thornley secondary electron detector and with the beam accelerating voltage kept at 20 kV. The topography of surfaces was inspected by atomic force microscope (AFM) (Nanosurf EasyScan 2) in the contact mode regime. The 2Au@Ti sample was measured in aberration corrected high-resolution transmission electron microscope (TEM) (JEOL ARM 200F) equipped with an EDX (energy-dispersive X-ray) detector. The preparation of cross-section lamellas for TEM was carried out using a focused ion beam system (JEOL JIB-4000). During this process, the current of gallium ions and acceleration voltages were adjusted, from 23 pA to 10 nA and from 3 to 30

kV, respectively. Prior to ion milling, the region of interest was carefully coated to avoid ion damage, following the procedure described elsewhere [30].

2.4. Electrochemical Setup

Cyclic voltammetry (CV), chronoamperometry (CA) and electrochemical impedance spectroscopy (EIS) were performed in a standard 3-electrode cell using AutoLab PGStat 302N potentiostat − galvanostat. Ag/AgCl KCl sat. and Pt mesh were used as reference and counter electrode, respectively. The electrolyte was composed of 0.1 M PBS pH 6. In the case of measurements at different pHs (Figure 7), 0.1 M Britton Robinson Solution (BRBS) was used. Electrolytes were deaerated with N_2 or Ar or saturated with oxygen before electrochemical measurement. The impedance spectra were recorded in 5 mM $K_3Fe(CN)_6$ + $K_4Fe(CN)_6$ in the frequency range from 20 kHz to 0.1 Hz using the signal amplitude of 10 mV and at the OCP. The fitting procedure was carried out with the use of EIS Analysis [31] using Powell algorithm and on the basis of the proposed electric equivalent circuits described in supporting information (Figures S1 and S2). Values obtained for all the elements present in the used electric equivalent circuit together with the goodness of fitting are set in Tables S1 and S2.

In order to precisely define the electrochemical activity of all electrodes listed in Table 1, the current was calculated and reported according to 3 options. In the option (1) the current is given as the direct measure in A (Figures 5, 6). In the option (2), the current is reported as the percentage between the actual current (i_x) and the maximum current (i_{max}) value registered at a particular condition. In the case of pH dependent measurements, i_{max} was the highest for pH 6 and therefore was chosen for calculation (Figure 7). To evaluate the stability of the gold containing nanostructured electrode modified with BOD in high ionic strength conditions, CA measurements were recorded without and in the presence of successive addition of Na_2SO_4 to PBS electrolyte. The measured current was divided by the initial value of current (i_0) recorded at the beginning of the experiment (Figure 11). In the option (3), the current is reported as a current density considering either the gold geometric area (Figures 8, 9 and 10).

2.5. CV fitting

The CVs were fitted to the steady-state models which considered the dispersion of enzyme orientations (βd_0 parameter) on the surface and the kinetics of the heterogeneous electron transfer (k^0 constant) (Equation (1)). Since the current for BOD-M-2Au@Ti demonstrated an almost straight line, it was not possible to fit it reliably to the same equation than BOD-M-

5Au@Ti and BOD-M-10Au@Ti and therefore another equation considering an infinite dispersion of the orientations ($\beta d_0 \to \infty$) was used (Equation (2)) [32].

$$i = \frac{i_{lim}^{red}}{a} \times \left[1 + \frac{1}{\beta d_0} ln \frac{a + \frac{b}{k_{OR}^0 / k_{red}}}{a + \frac{b \times \exp(\beta d_0)}{k_{OR}^0 / k_{red}}} \right] \quad (1)$$

$$i = \frac{i_{lim}^{red}}{\beta d_0} \frac{1}{a} \times ln\left(1 + \frac{a}{b} \frac{k_{OR}^0}{k_{red}}\right) \quad (2)$$

Where:

$$a = 1 + e_{OR} = 1 + \exp\left(\frac{F}{RT}\left(E - E_{ox/R}^0\right)\right)$$

$$b = e_{OR}^{\alpha} = e_{OR}^{1/2} = \exp\left(\frac{F}{2RT}\left(E - E_{ox/R}^0\right)\right)$$

3. Results and discussion

3.1. Optimizing the Au layer thickness to control the size of Au nanoparticles

Due to the anodization and etching procedure, nanodimpled titanium foil with an average diameter of one nanodimple reaching ca. 90 nm was received. This nanostructured titanium is serving as a substrate ensuring spatial ditribution of AuNPs formed out of the thin gold film. As can be seen from SEM images (Figure 1), the size and spatial distribution of AuNPs depend on the initial Au layer thickness. The usage of the thickest Au layer of 15 nm led to the production of agglomerates looking as gold microislands that are randomly distributed over the substrate, providing an inhomogeneous material. For the three other materials, namely 2Au@Ti, 5Au@Ti and 10Au@Ti, the distribution of AuNP is homogeneous. Magnetron sputtering of 2, 5 nm or 10 nm gold layer thickness followed by thermal treatment allows obtaining single gold nanoparticles, although some gold nanoparticles can be linked forming the shape remaining string with beads. Figure 2 shows the size distribution of AuNPs for these three materials. In the case of 2Au@Ti, a diameter of 13±6 nm is obtained (Figure 2). The thicker the Au layer is, the bigger the diameter of the nanoparticles reaching 46±12 nm for 5Au@Ti. For 10 nm gold thickness, single nanoparticles with a diameter of 81±13 nm are formed. One main objective here was to obtain AuNPs with size close to enzyme dimension (less than 10 nm diameter range) with the ultimate goal of fixing only one enzyme molecule per AuNP. *Mv* BOD for O_2 redution has molecular size 4×5×6 nm, meaning that 2Au@Ti should be the most suitable for our fundametal purpose [33]. To be noted also, the AuNP size

obtained in the current work are smaller than those previously obtained by laser ablation of gold films where the average size was superior to 110 nm [26].

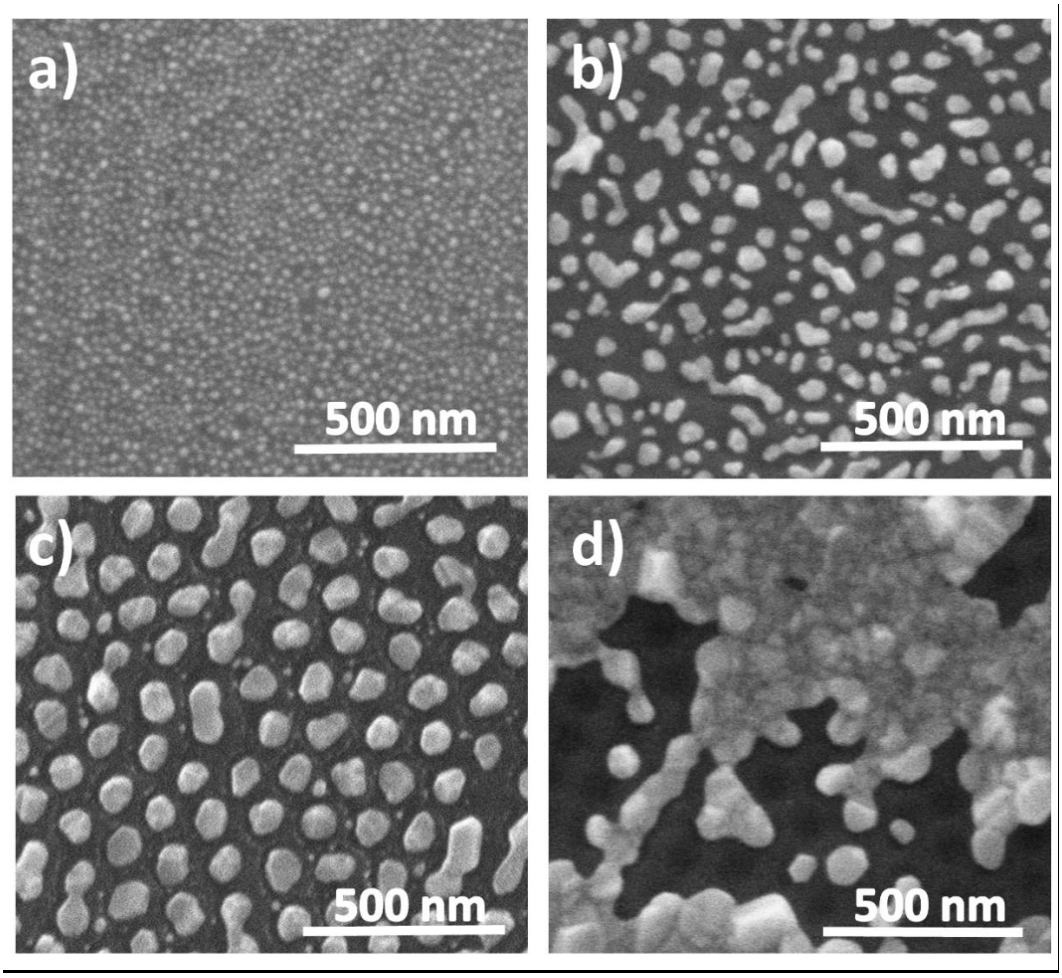

Figure 1. SEM images of a) 2Au@Ti, b) 5Au@Ti, c) 10Au@Ti, d) 15Au@Ti.

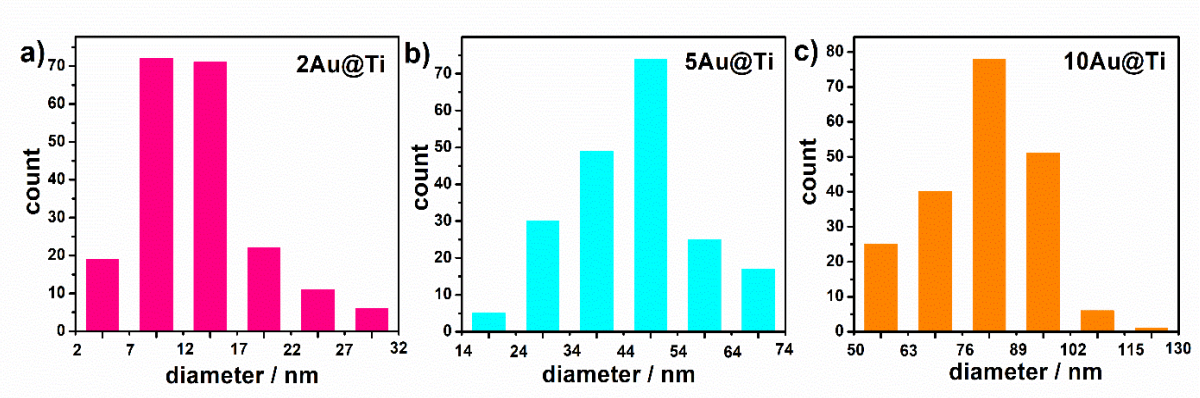

Figure 2. Size distribution of AuNPs for a) 2Au@Ti, b) 5Au@Ti, c) 10Au@Ti electrode.

More information about the structuration of AuNPs formed on nanostructured titanium foil is provided by AFM images (Figure 3). In the case of the 2Au@Ti (Figure 3a), Ti

nanodimpled platform is still visible, in contrast to larger nanoparticles (Figures 3b, 3c and 3d for 5Au@Ti, 10Au@Ti, 15Au@Ti). In the cases of the 5Au@Ti (Figure 3b) and the 10Au@Ti (Figure 3c), nanoparticles are uniformly distributed over the whole sample, in agreement with previously shown SEM images (Figure 1). For the 15Au@Ti (Figure 3d), gold nanoislands are inhomogeneously distributed, also in agreement with SEM pictures. AuNPs can be recognized as elements protruding from the electrode surface.

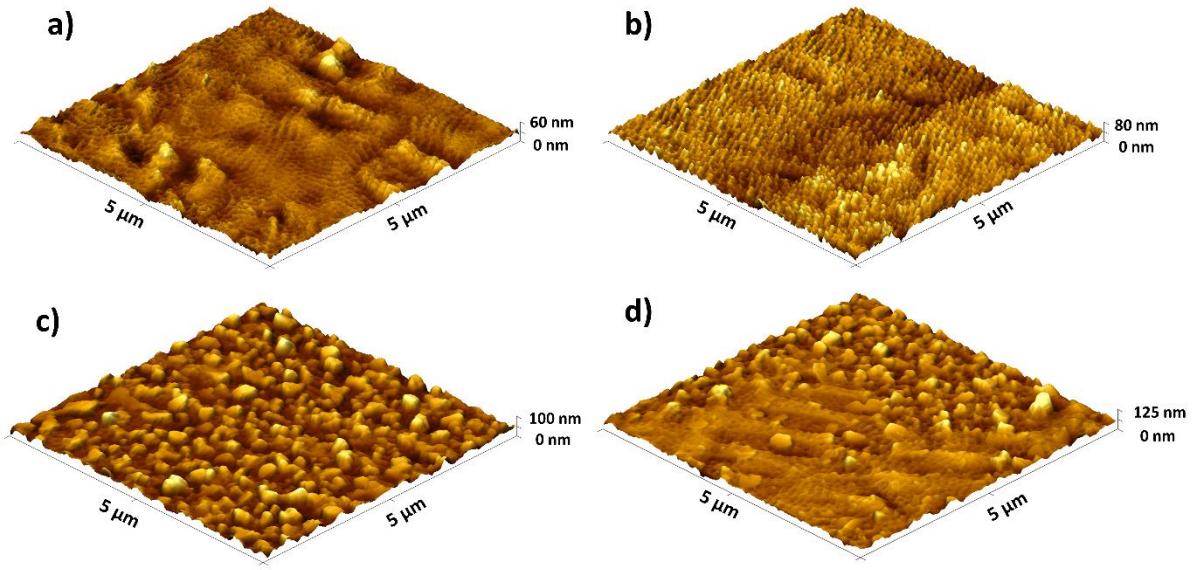

Figure 3. AFM images of a) 2Au@Ti, b) 5Au@Ti, c) 10Au@Ti, d) 15Au@Ti.

The size of NPs from 2Au@Ti compared to the dimple size raises the question of their spatial distribution and chemical composition. TEM pictures for the 2Au@Ti electrode presented in Figure 4 provide relevant information. The nanostructured titanium substrate is clearly imaged in the form of regularly spaced dimples with a depth of ca. 25 nm and a diameter of ca. 90 nm (Figure 4a). The Ti is covered by a thin 15 nm titanium oxide layer. During annealing, not only AuNPs but also the TiO_2 layer is formed in the closest surrounding of the nanoparticle as a result of exposition to oxygen containing atmosphere during thermal treatment. A large number of white spots can be obseved on Figure 4b which corresponds to AuNPs with diameters from 10 to 15 nm consistent with SEM observation. EDX maps confirm the presence of gold nanoparticles mainly at the bottom part of Ti nanodimples (Figure 4c). Some AuNPs are also visualized on the upper edges of dimples (as marked with a red arrow in Figure 4c). Actually, the diameter of nanoparticles obtained from 2 nm thick gold film (13±6 nm) is significantly smaller than the Ti nanodimple (ca. 90 nm). Consequently, NPs can enter

the dimple, covering the bottom part but also partially the edges, leaving the dimple visible as highlighted by AFM.

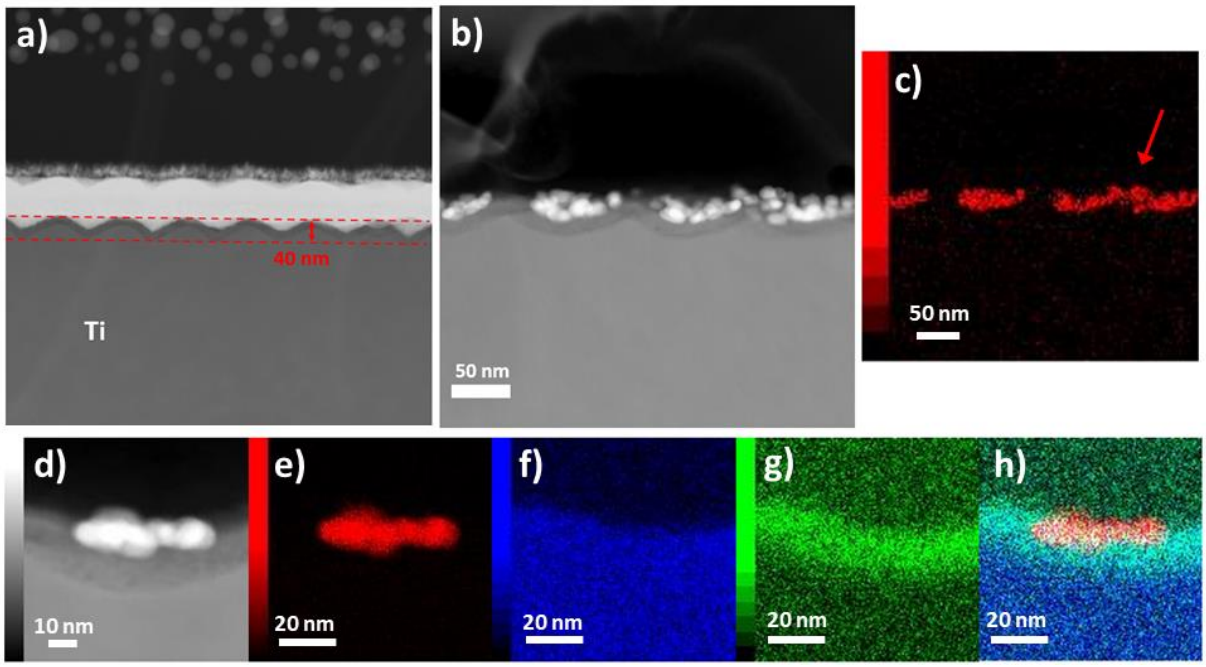

Figure 4. TEM images of the 2Au@Ti electrode (a, b, d) and EDX elemental mapping c, e) gold, f) titania, g) oxygen, h) Au, Ti, O elements.

The calculation of the electroactive surface areas assuming NPs are composed of pure gold (Figures S2 and S3, Table S3) highlights that A_{elec} is significantly lower than A_{total} for 2Au@Ti. Also, with the significant decrease of NP diameter deposited on TiO_2/Ti substrate, the electrochemical features arising on CV scans tend to semiconductor behavior. Indeed, in our experimental conditions, TiO_2 layer which is present between gold nanostructures is expected to interact more significantly with the smallest NPs [34, 35]. Not only such a configuration might induce an underestimated surface, but it is expected to impact the reactivity of AuNPs as further demonstrated below.

3.2. Selectivity of AuNP over Ti for enzymatic oxygen reduction

To get more insight in Ti-based surface chemical modification and further bioelectrocatalysis, CV and EIS measurements in 5 mM $K_3Fe(CN)_6$ + $K_4Fe(CN)_6$ in 0.1 M PBS solution were recorded (Figure 5). The 10Au@Ti electrode was chosen for this study since it exhibits the highest degree of AuNPs ordering. Electron transfer between the redox couple and the electrode occurs only after treatment of the semiconductor surface by gold nanostructure (Figures 5a and 5c). After each modification step of AuNPs, the electron transfer is slowed down as a consequence of 6-MHA modification, then BOD immobilization [28, 36].

Accordingly, after each modification step the electron-transfer resistance R2 increases (Figure 5d, Table S1) which confirms succesful binding between AuNP and 6-MHA as well as 6-MHA and BOD.

For the Ti and Ti modified electrodes (Figures 5a and 5b, Table S2), changes in Warburg parameter (W) should be considered. Indeed, because TiO_2 is a semiconductor material, it is not able to carry out the reversible redox reaction (as seen in Figure 5a). It can only absorb or modify those redox species reaching the electrode surface. Therefore changes in the Warburg parameter can provide information about potential absorption layers. The Warburg parameter W increases ca. 2 times after modification of Ti by either 6-MHA or BOD (Table S2). It does not change after BOD incubation in thiol-modified Ti (BOD-M-Ti electrode). This strongly suggests that both 6-MHA or BOD can adsorb on Ti, but BOD cannot be adsorbed on the thiol layer formed on Ti, possibly because of the inappropriate positioning of functional groups.

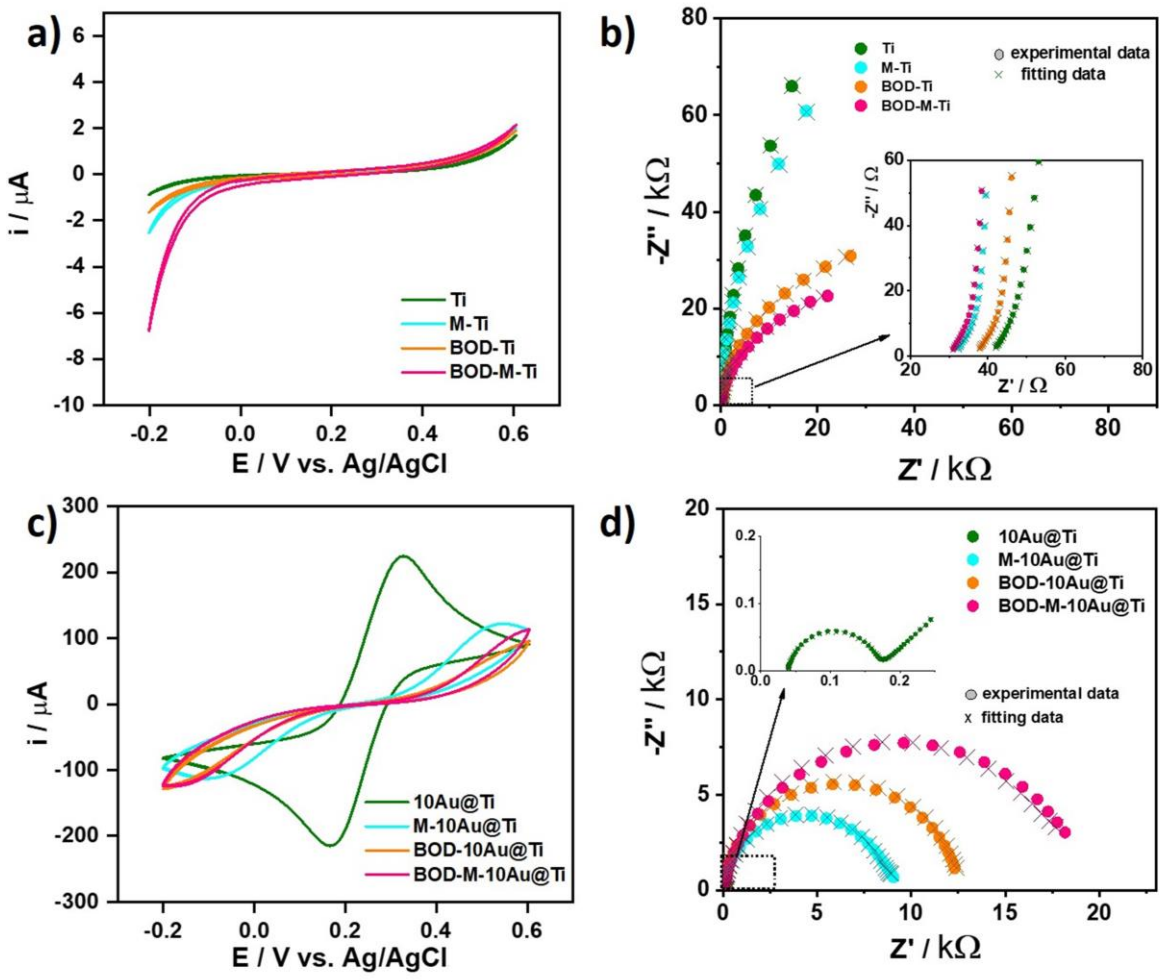

Figure 5. CVs curves (scan rate 10 mV/s) of a) Ti and Ti modified electrodes, and c) 10Au@Ti and 10Au@Ti

and impedance spectra of b) Ti and Ti modified electrode, and d) 10Au@Ti and 10Au@Ti modified electrode in 5 mM $K_3Fe(CN)_6 + K_4Fe(CN)_6$ in 0.1 M PBS. In EIS spectra dots represent experiental data while crosses are data received from the modelling procedure based on the proposed electric equivalent circuit (see SI for details).

To further verify the selectivity of gold NPs over the Ti/TiO_2 electrode surface for bioelectrocatalysis, the bare Ti dimpled foil was modified by 6-MHA and after incubation with *Mv* BOD CVs were performed in 0.1 M PBS (Figure 6). CV curves almost overlap no matter of the presence or not of O_2 in the electrolyte, indicating that Ti alone is not able to undergo any enzymatic reduction of O_2. Interestingly, this behavior is opposite to the case when ITO was used as a substrate for BOD anchoring [26]. The lack of bioelectrocatalysis on Ti surface may result either from the abscence of BOD or from an unfavorable orientation of BOD for direct catalysis. While 6-MHA can readily form SAMs on gold [37], ITO substrate or copper selenide quantum dots [38], no report showing successful modification on Ti or TiO_2 substrate was reported. As was indicated by Trino et al., bonding of acid containing –SH group onto the titanium dioxide surface may occur only through the grain boundaries due to the higher surface energy in those regions [39]. Such a property would not favour DET orientation of BOD. One advantage is that the catalytic signals that will be recorded thereafter will be exclusively linked to the presence of AuNPs.

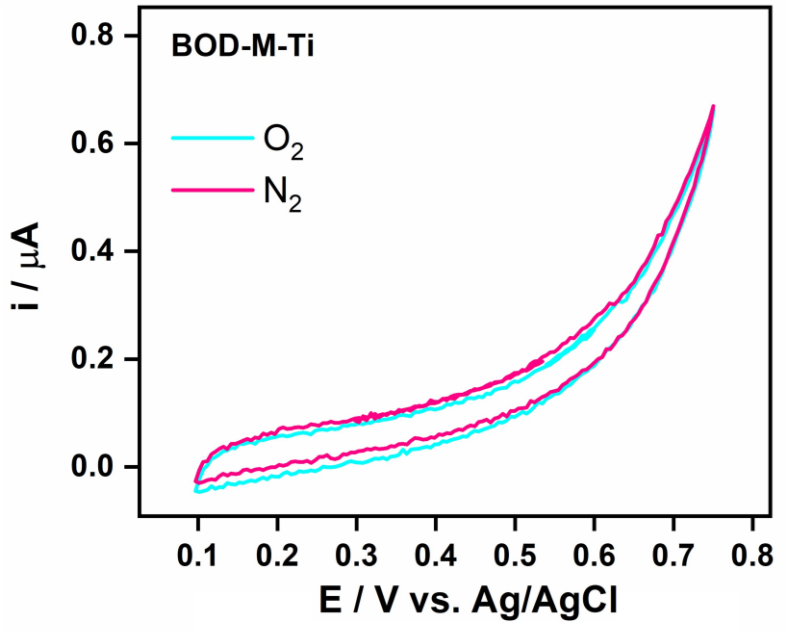

Figure 6. CVs curves of the BOD-M-Ti electrode modified by 100 µM BOD in 0.1 M PBS deareated with N_2 (pink curve) and saturated with O_2 (blue curve) (scan rate 10 mV/s).

3.3. Enzymatic O_2 reduction on XAu@Ti electrodes

O_2 reduction by *Mv* BOD absorbed on SAM-modified AuNPs deposited on dimple titanium foil in different pH electrolytes was first carried out. It is widely reported that the electrocatalytic activity of enzymes is strongly dependent on pH values [23]. The aim of this preliminary study was to investigate whether main well known electroenzymatic properties are maintained on substrate containing titanium, which has never been reported so far. The BOD-M-10Au@Ti electrode was chosen as a reference electrode due to its configuration of one AuNP per one Ti dimple exhibiting high degree of ordering. Figure 7 presents pH dependence of enzymatic ORR occurring at the BOD-M-10Au@Ti electrode. Measurements were carried out in 0.1 M Britton Robinson Solution in the range pH 4 to 7. For all pHs, a catalytic response was obtained in the presence of O_2. The highest current for ORR was obtained for pH 6 (Figure 7c), and the lowest one for pH 7 (Figure 7d). The pH-electrocatalysis relationship obtained is very similar to previously reported data at 6-MHA modified gold disk electrodes [23]. Such responses have been assigned to pH-dependent changes in intrinsic activity of enzyme as well as electrostatic interactions between *Mv* BOD and SAMs [23]. The onset potentials vs RHE for the four pH investigated are gathered in Table S4. Whereas a similar potential is obtained at pH 6 and pH 7, a 20-30 mV/UpH deviation is measured at more acidic pHs. Actually, the evolution of onset potentials with pH is admitted in the literature to be linked to BOD CuT1 potential changes. For BOD from *Magnaporthe oryzae*, Al-Lolage et al. reported a two slope behavior with a pH shift in the pH 6-7.6 range corresponding to a 1 e^-/1 H^+ process, while a sub-Nerstian response was obtained in the pH 4-6 range [7]. This variation agrees with the current study, and in accordance with the literature, we stated that such variation could be attributed to protonation/deprotonation of amino acid residues in the vicinity of Cu T1 [40].

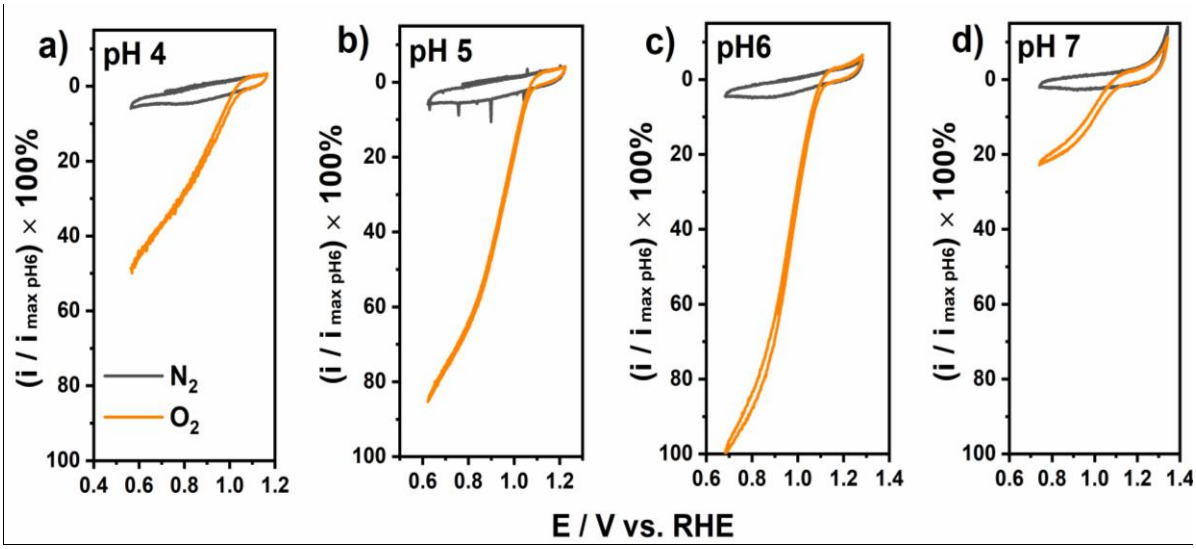

Figure 7. CV curves of the BOD-M-10Au@Ti electrode modified by 20 µM BOD at different pH a) pH 4, b) pH 5, c) pH 6, d) pH 7, 0.1 M Britton Robinson Solution deareated with N_2 (black curves) and saturated with O_2 (orange curves) (scan rate 10 mV/s).

The electroactive properties of the different electrodes modified with the enzyme, namely BOD-M-2Au@Ti, BOD-M-5Au@Ti, BOD-M-10Au@Ti and BOD-M-Audisc electrodes were then investigated using CV in oxygenated 0.1 M PBS solution (Figure 8). Not only different sizes of nanoparticles but also various *Mv* BOD concentrations were investigated. Biocatalytic oxygen reduction occurs whatever the electrode type. For all the investigated electrodes, a bell-shape relation ship between the catalytic current and the enzyme concentration was obtained with the highest current recorded for 20 µM BOD. This tendency has been already reported on other materials, and could be explained by changes in enzyme conformation in a crowding enironment [24]. The ORR onset potential for the BOD-M-2Au@Ti, BOD-M-5Au@Ti, and BOD-M-10Au@Ti reaches ca. 1.13 V, whereas, in the case of BOD-M-Audisc electrode it is 1.10 V vs. RHE. By comparing the current densities reported to the geometric surface areas at BOD-M-Audisc (Figure S4) and at BOD-M-5Au@Ti and BOD-M-10Au@Ti for 20 µM BOD, an enhancement of 2.5 and 3 times is obtained respectively, while the current profile for BOD-M-2Au@Ti is very similar to that of BOD-M-Audisc.

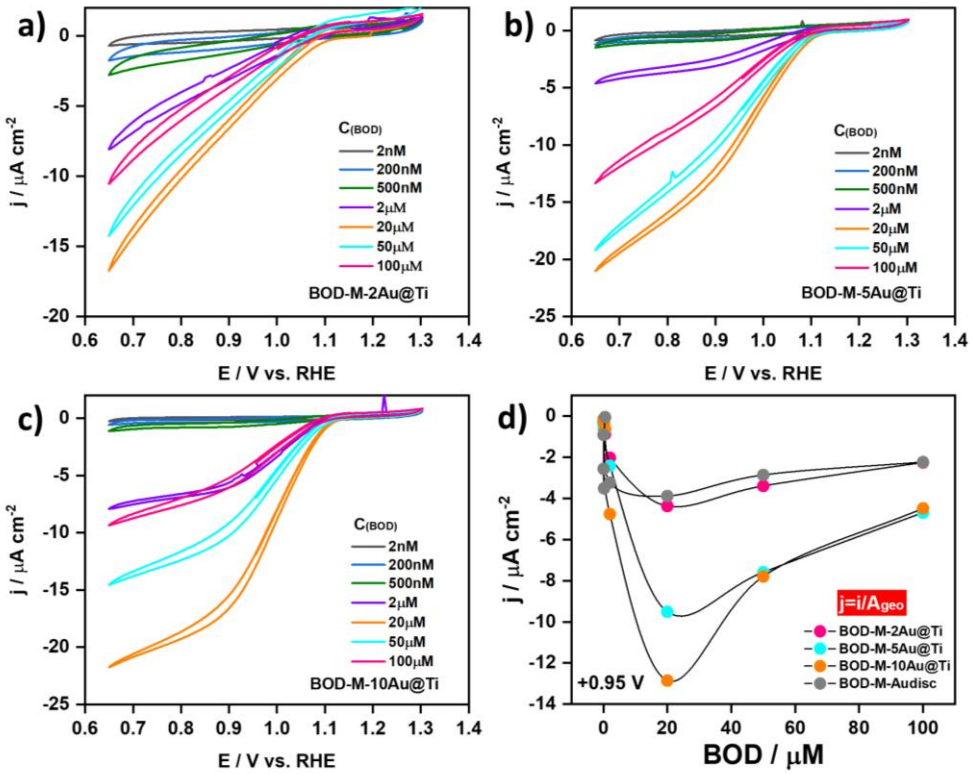

Figure 8. CVs curves of a) BOD-M-2Au@Ti, b) BOD-M-5Au@Ti, c) BOD-M-10Au@Ti electrode as a function of increasing *Mv* BOD concentrations in 0.1 M PBS saturated with O_2 (scan rate 10 mV/s), d) relationship between catalytic current density reported to the geometric surface area and enzyme concentration at the potential of +0.95 V vs RHE.

To be noted, in addition to weakly enhanced catalytic currents in the case of BOD-M-2Au@Ti, the CV shapes also significantly differ from those at BOD-M-5Au@Ti and BOD-M-10Au@Ti. No plateau can be reached in the cathodic regime, and the CV curve displays an almost straight line behavior. With this specific material, the shape of the CV curves and the magnitude of the catalytic current is also little affected by 6-MHA modification (Figure 9a). This contrasts with the marked increase in current and CV shape turning to a narrower distribution of electron transfer rates when both 5Au@Ti and 10Au@Ti are modified by the thiol before incubation in BOD solution (Figures 9b and 9c) [23].

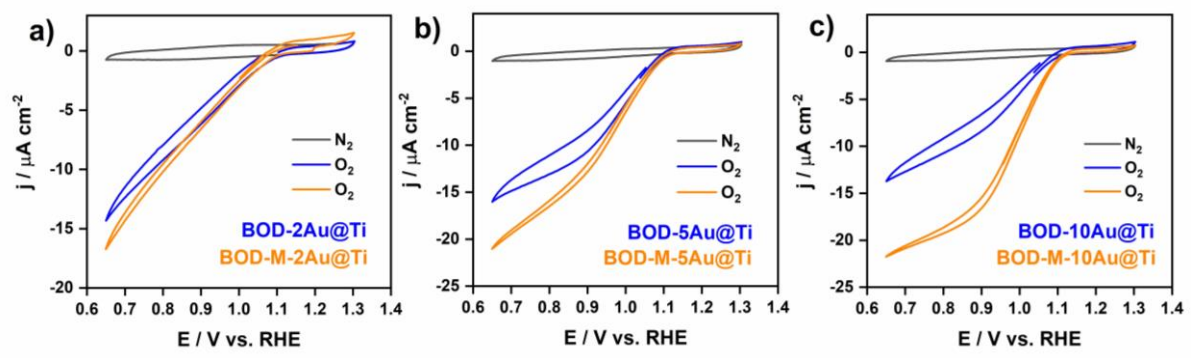

Figure 9. CVs curves of a) 2Au@Ti, b) 5Au@Ti, c) 10Au@Ti electrodes modified by 20 µM BOD in 0.1 M PBS saturated with O_2 without (blue curves) or with (orange curves) thiol modification. Black curve is assigned to the BOD-XAu@Ti electrode under N_2. Scan rate 10 mV/s.

As noted above, the semiconducting properties of TiO_2 alter those of the smallest AuNPs. It was reported that changes in local charge distribution occur on AuNPs interacting with TiO_2 semiconductor [41]. Such charge distribution results from electron injection from the n-type semiconductor supporting material. Moreover, decreasing nanoparticle size, the surface energy density increases owing to formation of high-energy electrons (hot electrons) localised at the NPs [42]. In addition, the role of quantum size effect on electronic properties based on density functional theory simulations predicts spill-out of electrons outside the nanoparticle and change of its dielectric properties at the surface. Quantum size effect can occur for nanoparticles with diameter of ~ 10 nm [43]. Therefore, 2Au@Ti NPs with a thickness ratio of Au to TiO_2 lower than in the cases of 5Au@Ti and 10Au@Ti samples are negatively charged (Scheme 2). This specific charge distribution tends to repel the negatively charged 6-MHA, precluding SAM formation and disfavoring favorable BOD orientation for direct bioelectrocatalysis.

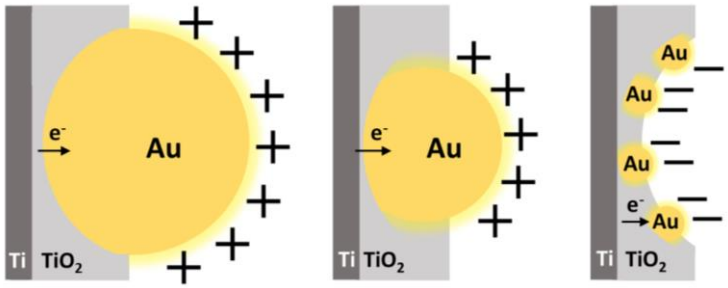

Scheme 2. Schematic representation of the charge distribution over 10Au@Ti, 5Au@Ti and 2Au@Ti electrodes.

An alternative explanation may arise from prevalent semi-conducting properties of 2Au@Ti material. The electrochemical behavior of $FeCN_6^{3-}$ and $Ru(NH_3)_6^{3+}$ redox probes were

run on 2Au@Ti, 5Au@Ti and 10Au@NP at different scan rates (Figure S6). Whereas $FeCN_6^{3-}$ behaves as a quasi-reversible electrochemical couple on 5Au@Ti and 10Au@Ti with peak potential differences about 120 mV at 100 mV/s, the shape of the CV at 2Au@Ti reveals a very slow electron transfer process. Such a modification in the electron transfer rate could be induced by the negative charge of the 2Au@Ti NP. However, the electron transfer process is also affected in the case of $Ru(NH_3)_6^{3+}$, with furthermore no increase in the current magnitude on the smallest NPs as would have been expected in case of favorable attraction. These data support the prevalent effect of AuNP/TiO_2 interactions which affects the electron transfer rate, the greatest in the case of 2Au@Ti NPs. A direct consequence is that the evolution of catalytic currents reported versus the electroactive area (Figure S5) which suggests that 2Au@Ti should be much more efficient than the bigger particle sizes, is instead a consequence of Au/TiO_2 interaction that induced an under-estimation of the electroactive surface area.

Fitting of the CVs (Figure 10 and Table 2) obtained with BOD-M-2Au@Ti, BOD-M-5Au @Ti and BOD-M-10Au@Ti leads to additional information. In the cases of BOD-M-5Au@Ti and BOD-M-10Au@Ti, the βd_0 orientation parameter takes values of 9.1 and 6.5 while the ratio of k_0/k_{cat} are respectively 19 and 14. These values are in agreement with a quite narrow orientation of the enzyme on the thiol-modified materials [23]. On the other hand, the CV curve for the BOD-M-2Au@Ti can only be fit with a model where βd_0 tends to infinity, and k_0/k_{cat} is decreased to 1, i.e. one order of magnitude smaller than for the higher size NPs. Since k_{cat} is not expected to vary since the same enzyme is used, this suggests a decrease in the interfacial electron transfer rate constant induced by the presence of TiO_2 in the surrounding of the AuNPs. The increase of βd_0 for the smallest NPs can be explained either by the increase of distance distribution d_0 between enzyme active centre and the gold surface because of the absence of thiol linker, or by the increase of β, an exponential decay constant dependant on the nature of the space between the active centre and the electrode. A thin isolating layer of TiO_2 in the close surrounding of the gold NPs as demonstrated by TEM images would increase the potential energy barrier that electron needs to overcome and thus would increase β.

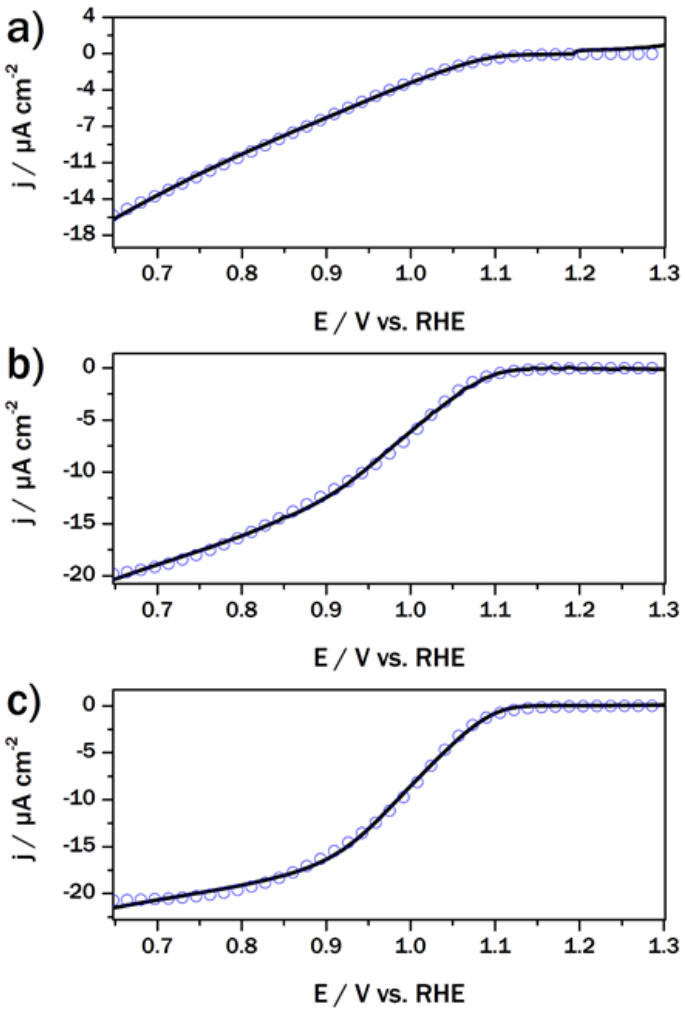

Figure 10. Electrocatalytic curves of a) BOD-M-2Au@Ti, b) BOD-M-5Au@Ti, c) BOD-M-10Au@Ti electrode with subtracted blank and fitted to the equation 2 (a) or 1 (b,c).

Table 2. Parameters derived from the fitting

Parameter	BOD-M-2Au@Ti		BOD-M-5Au@Ti		BOD-M-10Au@Ti	
	Value	Error	Value	Error	Value	Error
$I_{lim}, \mu A/cm^2$	-	-	-29.4	0.17	-18.2	0.1
βd_0	> 9	-	9.1	0.2	6.5	0.3
$I_{lim}/\beta d_0, \mu A/cm^2$	-16.6	0.15	-	-	-	-
k^0_{max}/k_{cat}	1.0	0.2	19	2	14	3

3.5. Stability of BOD-M-10Au@Ti in the presence of high salt concentration

To explore further the capacity of 10Au@Ti to support efficient bioelectrocatalysis, we studied the impact of salt additions on the bioelectrocatalysis. Indeed, using high electrolyte concentrations is often a key in bioelectrocatalysis to overcome local pH changes [44, 45]. We recently reported the complex effect of increasing concentrations of salts on ORR by *Mv* BOD immobilized on CNT films or on thiol-modified gold electrodes [46]. We especially highlighted the reversible flipping of the protein on a SAM-modified gold disk electrode surface when electrostatic interactions were decreased by addition of salts at concentrations higher than 1 M. We also highlighted that whereas the catalytic current decreases with salt addition with the enzyme adsorbed on thiol-based planar gold electrodes, it increases when the protein is covalently attached. Enzyme compaction in the presence of high salt concentrations which decreases the distance between Cu T1 and the electrode was proposed to explain this last phenomenon.

Immobilization of the enzyme on AuNPs is expected to change the nature of electrode/protein interactions, hence modifying the effect of salt addition. Chronoamperometry measurements were then carried at the potential of +0.43 V vs. Ag/AgCl with the successive addition of Na_2SO_4 solution to PBS (Figure 11). As previously reported, the current recorded for BOD-M-Audisc electrode decreases upon stepwise increase of Na_2SO_4 content in PBS, being 40% of the initial current after 1 M salt addition. The same experiment conducted on BOD-M-10Au@Ti induces a completely different CA response. First of all, high stability of the current with time is observed before any salt addition. For salt concentrations in the range 100 mM to 400 mM, an increase in the catalytic current is observed. This step is followed by a slight decrease of the current, the remaining current at 1 M salt concentration being similar to the initial current. This enhanced stability of the nanobioelectrode is very attractive and may be related to NP surface curvature, that offers specific surface of contact for the enzyme [1]. Smaller area for protein contact compared to Audisc, as well as suppression of unfavorable protein–protein lateral interactions are most probably the reasons that can account for stabilization effect of AuNPs.

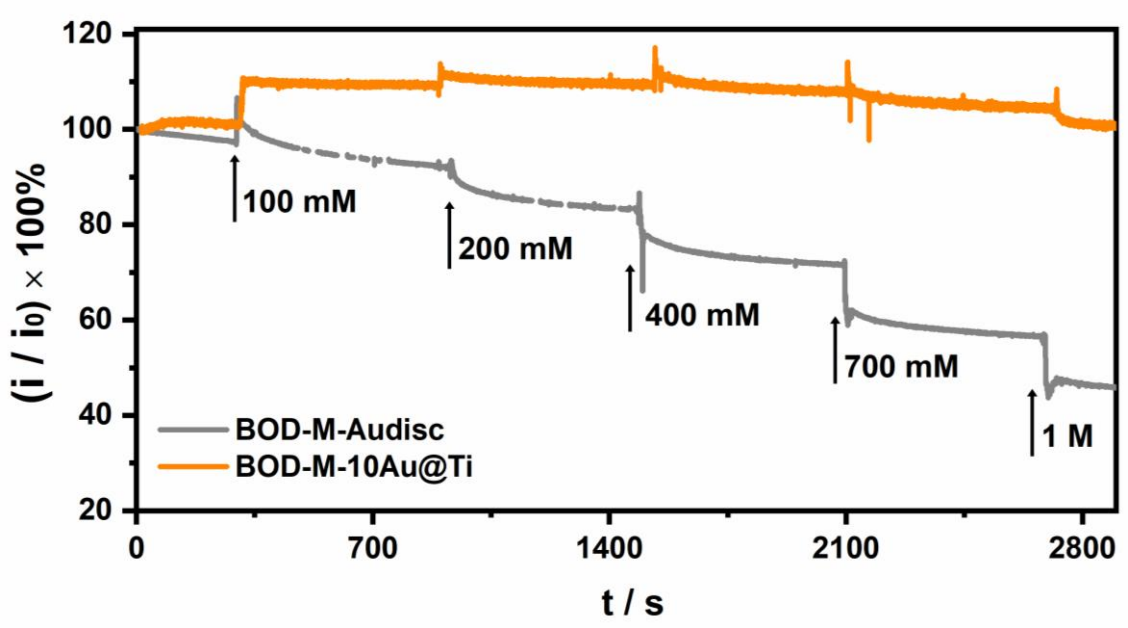

Figure 11. CA curves for the BOD-M-Audisc and BOD-M-10Au@Ti in 0.1 M PBS with addition of Na_2SO_4 saturated with O_2.

4. Conclusions

We investigated in this work the efficiency of enzymatic oxygen reduction once *Mv* BOD was immobilized on gold nanoparticles (AuNPs) spatially distributed in Ti nanodimples. The used synthesis method allows to control the size of AuNPs and regularely distribute them on the conducting surface which is not easely achieved otherwise. The advantage of such construction was not only to investigate AuNPs with sizes from less than 100 nm down to 10 nm, but also to take benefit of the semi-conducting properties of TiO_2 allowing to restrict occurrence of biocatalysis only on AuNPs. We showed that biggest AuNPs enhanced the current density by more than 2 times. However, we also demonstrated that surrounding of the smallest AuNPs with a layer of TiO_2 induced a modification in the electron transfer process most probably related to the decrease of the interfacial electron transfer rate k^0 and an increase in the constant decay parameter β. This means that the use of AuNPs via the Ti nanodimple method requires a balance between efficient size for biocatalysis and impact of TiO_2 layer. High stability of the enzymatic current was obtained in the presence of high concentration of salts. This finding is very interesting in view of applications which require high ionic strength to mitigate any local pH changes. In depth studies are now required to search for the reasons for such a stabilization.

CRediT authorship contribution statement

Wiktoria Lipinska: electrode fabrication, electrochemical measurements, SEM, AFM and TEM image analysis, original draft writing. **Vita Saska**: electrochemical measurements. **Jakub Karczewski** : SEM and AFM measurements. **Emerson Coy** : TEM measurements. **Katarzyna Siuzdak**: TEM measurements, methodology, supervision, review & editing. **Ievgen Mazurenko**: Modeling of the CV curves. **Elisabeth Lojou**: conceptualization, methodology, supervision, review & editing. All authors participated in the discussion of results and edition of the final version of the manuscript.

Acknowledgments

Research is financed by National Science Centre (Poland): Grant No. 2019/35/N/ST5/02604 and ANR (ENZYMOR-ANR-16-CE05- 0024).

Declaration of Competing Interest

The authors declare that they have no known competing financial interests or personal relationships that could have appeared to influence the work reported in this paper.

References

[1] C. Beaufils, H.M. Man, A. de Poulpiquet, I. Mazurenko, E. Lojou, From Enzyme Stability to Enzymatic Bioelectrode Stabilization Processes, Catalysts, 11 (2021).
[2] K. Kano, Fundamental insight into redox enzyme-based bioelectrocatalysis, Biosci. Biotechnol. Biochem., 86 (2022) 141-156.
[3] N. Mano, A. de Poulpiquet, O2 Reduction in Enzymatic Biofuel Cells, Chem. Rev., 118 (2018) 2392-2468.
[4] O. Aleksejeva, I. Mateljak, R. Ludwig, M. Alcalde, S. Shleev, Electrochemistry of a high redox potential laccase obtained by computer-guided mutagenesis combined with directed evolution, Electrochem. Commun., 106 (2019).
[5] Y. Zhang, Z.Y. Lv, J. Zhou, F.X. Xin, J.F. Ma, H. Wu, Y. Fang, M. Jiang, W.L. Dong, Application of eukaryotic and prokaryotic laccases in biosensor and biofuel cells: recent advances and electrochemical aspects, Appl. Microbiol. Biotechnol., 102 (2018) 10409-10423.
[6] I. Mazurenko, T. Adachi, B. Ezraty, M. Ilbert, K. Sowa, E. Lojou, Electrochemistry of copper efflux oxidase-like multicopper oxidases involved in copper homeostasis, Curr. Op. Electrochem., 32 (2022).
[7] F.A. Al-Lolage, P.N. Bartlett, S. Gounel, P. Staigre, N. Mano, Site-Directed Immobilization of Bilirubin Oxidase for Electrocatalytic Oxygen Reduction, ACS Catal., 9 (2019) 2068-2078.
[8] A. de Poulpiquet, C.H. Kjaergaard, J. Rouhana, I. Mazurenko, P. Infossi, S. Gounel, R. Gadiou, M.T. Giudici-Orticoni, E.I. Solomon, N. Mano, E. Lojou, Mechanism of Chloride Inhibition of Bilirubin Oxidases and Its Dependence on Potential and pH, ACS Catal., 7 (2017) 3916-3923.
[9] S. Gentil, M. Carriere, S. Cosnier, S. Gounel, N. Mano, A. Le Goff, Direct Electrochemistry of Bilirubin Oxidase from Magnaporthe orizae on Covalently-Functionalized MWCNT for the Design of High-Performance Oxygen-Reducing Biocathodes, Chemistry-a Eur. J., 24 (2018) 8404-8408.
[10] A. Sekretareva, S.L. Tian, S. Gounel, N. Mano, E.I. Solomon, Electron Transfer to the Trinuclear Copper Cluster in Electrocatalysis by the Multicopper Oxidases, J. Am. Chem. Soc., 143 (2021) 17236-17249.

[11] S.M. Jones, E.I. Solomon, Electron transfer and reaction mechanism of laccases, Cell. Mol. Life Sci., 72 (2015) 869-883.
[12] I. Mazurenko, V.P. Hitaishi, E. Lojou, Recent advances in surface chemistry of electrodes to promote direct enzymatic bioelectrocatalysis, Current Opinion in Electrochemistry, 19 (2020) 113-121.
[13] M. Tominaga, S. Tamai, S. Nakao, M. Miyamoto, T. Satomura, High electrochemical stability of hyperthermophilic archaeal multicopper enzyme adsorbed on gold electrodes compared to fungal laccase, Electrochem. Commun., 136 (2022).
[14] N. Lalaoui, K. Gentil, I. Ghandari, S. Cosnier, F. Giroud, Nitrobenzoic acid-functionalized gold nanoparticles: DET promoter of multicopper oxidases and electrocatalyst for NAD-dependent glucose dehydrogenase, Electrochim. Acta, 408 (2022).
[15] Y. Takahashi, M. Wanibuchi, Y. Kitazumi, O. Shirai, K. Kano, Improved direct electron transfer-type bioelectrocatalysis of bilirubin oxidase using porous gold electrodes, Journal of Electroanalytical Chemistry, 843 (2019) 47-53.
[16] V.P. Hitaishi, R. Clement, N. Bourassin, M. Baaden, A. de Poulpiquet, S. Sacquin-Mora, A. Ciaccafava, E. Lojou, Controlling Redox Enzyme Orientation at Planar Electrodes, Catalysts, 8 (2018).
[17] W.Q. Chen, W.J. Wu, Y.Q. Yu, Y. Liu, F.L. Jiang, New Insights on the Size-Dependent Inhibition of Enzymes by Gold Nanoparticles, Langmuir, 39 (2023) 9595-9603.
[18] M. Kizling, M. Dzwonek, A. Wieckowska, R. Bilewicz, Gold nanoparticles in bioelectrocatalysis - The role of nanoparticle size, Curr. Op. Electrochem., 12 (2018) 113-120.
[19] S. Chumillas, B. Maestro, J.M. Feliu, V. Climent, Comprehensive Study of the Enzymatic Catalysis of the Electrochemical Oxygen Reduction Reaction (ORR) by Immobilized Copper Efflux Oxidase (CueO) From Escherichia coli, Frontiers in Chemistry, 6 (2018).
[20] V. Climent, Y.C. Fu, S. Chumillas, B. Maestro, J.F. Li, A. Kuzume, S. Keller, T. Wandlowski, Probing the Electrocatalytic Oxygen Reduction Reaction Reactivity of Immobilized Multicopper Oxidase CueO, J. Phys. Chem. C, 118 (2014) 15754-15765.
[21] C. Gutierrez-Sanchez, A. Ciaccafava, P.Y. Blanchard, K. Monsalve, M.T. Giudici-Orticoni, S. Lecomte, E. Lojou, Efficiency of Enzymatic O-2 Reduction by Myrothecium verrucaria Bilirubin Oxidase Probed by Surface Plasmon Resonance, PMIRRAS, and Electrochemistry, ACS Catal., 6 (2016) 5482-5492.
[22] M. Dagys, A. Laurynenas, D. Ratautas, J. Kulys, R. Vidziunaite, M. Talaikis, G. Niaura, L. Marcinkeviciene, R. Meskys, S. Shleev, Oxygen electroreduction catalysed by laccase wired to gold nanoparticles via the trinuclear copper cluster, Energ. Environ. Sci., 10 (2017) 498-502.
[23] V.P. Hitaishi, I. Mazurenko, M. Harb, R. Clement, M. Taris, S. Castano, D. Duche, S. Lecomte, M. Ilbert, A. de Poulpiquet, E. Lojou, Electrostatic-Driven Activity, Loading, Dynamics, and Stability of a Redox Enzyme on Functionalized-Gold Electrodes for Bioelectrocatalysis, ACS Catal., 8 (2018) 12004-12014.
[24] T. McArdle, T.P. McNamara, F. Fei, K. Singh, C.F. Blanford, Optimizing the Mass-Specific Activity of Bilirubin Oxidase Adlayers through Combined Electrochemical Quartz Crystal Microbalance and Dual Polarization Interferometry Analyses, ACS Appl. Mater. Inter., 7 (2015) 25270-25280.
[25] Y. Wu, N. Arroyo-Curras, Advances in nucleic acid architectures for electrochemical sensing, Curr. Op. Electrochem., 27 (2021).
[26] V.P. Hitaishi, I. Mazurenko, M.A. Vengasseril, A. de Poulpiquet, G. Coustillier, P. Delaporte, E. Lojou, Nanosecond Laser-Fabricated Monolayer of Gold Nanoparticles on ITO for Bioelectrocatalysis, Frontiers in Chemistry, 8 (2020).
[27] W. Lipinska, K. Siuzdak, J. Ryl, P. Barski, G. Sliwinski, K. Grochowska, The optimization of enzyme immobilization at Au-Ti nanotextured platform and its impact onto the response towards glucose in neutral media, Materials Research Express, 6 (2019).
[28] W. Lipinska, K. Siuzdak, J. Karczewski, A. Dolega, K. Grochowska, Electrochemical glucose sensor based on the glucose oxidase entrapped in chitosan immobilized onto laser-processed Au-Ti electrode, Sensors and Actuators B-Chemical, 330 (2021).

[29] W. Lipinska, J. Ryl, P. Slepski, K. Siuzdak, K. Grochowska, Exploring multi-step glucose oxidation kinetics at GOx-functionalized nanotextured gold surfaces with differential impedimetric technique, Measurement, 174 (2021).
[30] Y.C. Park, B.C. Park, S. Romankov, K.J. Park, J.H. Yoo, Y.B. Lee, J.M. Yang, Use of permanent marker to deposit a protection layer against FIB damage in TEM specimen preparation, Journal of Microscopy, 255 (2014) 180-187.
[31] A.S. Bondarenko, G.A. Ragoisha, Inverse problem in potentiodynamic electrochemical impedance, 3rd Winter School on Chemometrics (WSC-3) Pushkinskie Gory, RUSSIA, 2004, pp. 89-102.
[32] V. Fourmond, C. Leger, Modelling the voltammetry of adsorbed enzymes and molecular catalysts, Current Opinion in Electrochemistry, 1 (2017) 110-120.
[33] D. Pankratov, J. Sotres, A. Barrantes, T. Arnebrant, S. Shleev, Interfacial Behavior and Activity of Laccase and Bilirubin Oxidase on Bare Gold Surfaces, Langmuir, 30 (2014) 2943-2951.
[34] W. Lipinska, K. Grochowska, J. Ryl, J. Karczewski, K. Siuzdak, Influence of Annealing Atmospheres on Photoelectrochemical Activity of TiO2 Nanotubes Modified with AuCu Nanoparticles, ACS Appl. Mater. Inter., 13 (2021) 52967-52977.
[35] W. Lipinska, K. Grochowska, J. Karczewski, J. Ryl, A. Cenian, K. Siuzdak, Thermally tuneable optical and electrochemical properties of Au-Cu nanomosaic formed over the host titanium dimples, Chemical Engineering Journal, 399 (2020).
[36] D. Nidzworski, K. Siuzdak, P. Niedzialkowski, R. Bogdanowicz, M. Sobaszek, J. Ryl, P. Weiher, M. Sawczak, E. Wnuk, W.A. Goddard, A. Jaramillo-Botero, T. Ossowski, A rapid-response ultrasensitive biosensor for influenza virus detection using antibody modified boron-doped diamond, Scientific Reports, 7 (2017).
[37] J. Noh, K. Konno, E. Ito, M. Hara, Growth processes and control of two-dimensional structure of carboxylic acid-terminated self-assembled monolayers on Au(111), Japanese Journal of Applied Physics Part 1-Regular Papers Brief Communications & Review Papers, 44 (2005) 1052-1054.
[38] L.C. Pacoste, A.N. Jijana, U. Feleni, E. Iwuoha, Mercaptoalkanoic Acid-Induced Band Gap Attenuation of Copper Selenide Quantum Dot, Chemistryselect, 5 (2020) 4994-5005.
[39] L.D. Trino, E.S. Bronze-Uhle, A. George, M.T. Mathew, P.N. Lisboa, Surface Physicochemical and Structural Analysis of Functionalized Titanium Dioxide Films, Colloids and Surfaces a-Physicochemical and Engineering Aspects, 546 (2018) 168-178.
[40] S. Tsujimura, K. Murata, Electrochemical Oxygen Reduction Catalyzed by Bilirubin Oxidase with the Aid of 2,2 '-Azinobis(3-ethylbenzothiaZolin-6-sulfonate) on a MgO-template Carbon Electrode, Electrochim. Acta, 180 (2015) 555-559.
[41] M. McEntee, A. Stevanovic, W.J. Tang, M. Neurock, J.T. Yates, Electric Field Changes on Au Nanoparticles on Semiconductor Supports - The Molecular Voltmeter and Other Methods to Observe Adsorbate-Induced Charge-Transfer Effects in Au/TiO2 Nanocatalysts, J. Am. Chem. Soc., 137 (2015) 1972-1982.
[42] Y.X. Xie, J.J. Li, Z.L. Peng, Y. Yao, S.H. Chen, A first-principle study on the atomic-level mechanism of surface effect in nanoparticles, Materials Today Communications, 24 (2020).
[43] M.S. Tame, K.R. McEnery, S.K. Ozdemir, J. Lee, S.A. Maier, M.S. Kim, Quantum plasmonics, Nature Physics, 9 (2013) 329-340.
[44] B. Tassy, A.L. Dauphin, H.M. Man, H. Le Guenno, E. Lojou, L. Bouffier, A. de Poulpiquet, In Situ Fluorescence Tomography Enables a 3D Mapping of Enzymatic O-2 Reduction at the Electrochemical Interface, Analytical Chemistry, 92 (2020) 7249-7256.
[45] E.E. Moore, S.J. Cobb, A.M. Coito, A.R. Oliveira, I.A.C. Pereira, E. Reisner, Understanding the local chemical environment of bioelectrocatalysis, Proc. Nat. Ac. Sci. USA, 119 (2022).
[46] V. Saska, U. Contaldo, I. Mazurenko, A. de Poulpiquet, E. Lojou, High electrolyte concentration effect on enzymatic oxygen reduction, Bioelectrochem., 153 (2023) 108503.